Ultimate Bending Strength of Composite Beams[a]

By Ever J. Barbero,[1] Shin-Ham Fu,[2] and Ioannis Raftoyiannis[3]

Abstract: This paper deals with glass-fiber–reinforced plastic (GFRP) beams produced by the pultrusion process. Pultruded composite members are being used extensively as beams for structural applications. Widespread use is motivated primarily due to the light weight and corrosion resistance of composite materials. Low-cost, mass-produced pultruded beams are becoming competitive with conventional materials like steel and reinforced concrete. Common structural shapes have open or closed sections of thin composite walls. The ultimate bending strength of pultruded composite beams is limited by various failure mechanisms. Most failure modes are precipitated by local buckling of the thin walls. Analytical models for several local buckling modes are used in this work to model observed behavior in commercially available composite beams. Experimental data for composite beams are presented for comparison. Local buckling initiates a failure mode that eventually results in material degradation and total failure of the beam. Due to the large elongation to failure of the composite material, only postbuckling deformations can subject the material to deformations large enough to produce failure. Experimental results are shown to sustain these arguments. Analytical models for local buckling are developed and correlated with observed behavior.

Introduction

Conventional composite materials (e.g., reinforced concrete) have been used in the construction industry for many years because they perform better than the constituents themselves and better than competing homogeneous materials. Advanced composite materials like fiber-reinforced plastics (FRP) have been used primarily for aerospace applications. They offer many advantages over conventional materials, such as light weight and resistance to corrosion. Recently, low-cost polyester resins and glass-fiber–reinforced plastics (GFRPs) are being considered for infrastructural applications. Other constituents of relatively high cost (e.g., carbon fibers and thermoplastic resins) can also be used in limited quantities.

From a broad range of manufacturing techniques available for the production of advanced composite materials, pultrusion appears to be the best suited for infrastructural applications. In the pultrusion process, fibers are pulled through a bath of resin, then through a heated die that provides the shape of the cross section to the final product (Fig. 1). Pultrusion is a continuous process with an average output of 2 ft/min (61 cm/min) of prismatic sections of virtually any shape. Currently available shapes include I-beams up to 12 in. by 6 in. (30 cm by 15 cm), 6 in. by 4 in. (15 cm by 10 cm) box beams, and a variety of other shapes. The resin system can be

[a]Presented at the May 30th, 1990, Structures Congress, ASCE Structures Division, held at Baltimore, MD.

[1]Asst. Prof., Dept. of Mech. and Aerosp. Engrg., Constructed Facilities Ctr., West Virginia Univ., Morgantown, WV 26506-6101.

[2]Grad. Student, Dept. of Civ. Engrg., West Virginia Univ., Morgantown, WV.

[3]Grad. Student, Dept. of Civ. Engrg., West Virginia Univ., Morgantown, WV.

Note. Discussion open until April 1, 1992. To extend the closing date one month, a written request must be filed with the ASCE Manager of Journals. The manuscript for this paper was submitted for review and possible publication on May 23, 1990. This paper is part of the ***Journal of Materials in Civil Engineering***, Vol. 3, No. 4, November, 1991. ©ASCE, ISSN 0899 1561/91/0004-0292/$1.00 + $.15 per page. Paper No. 26354.

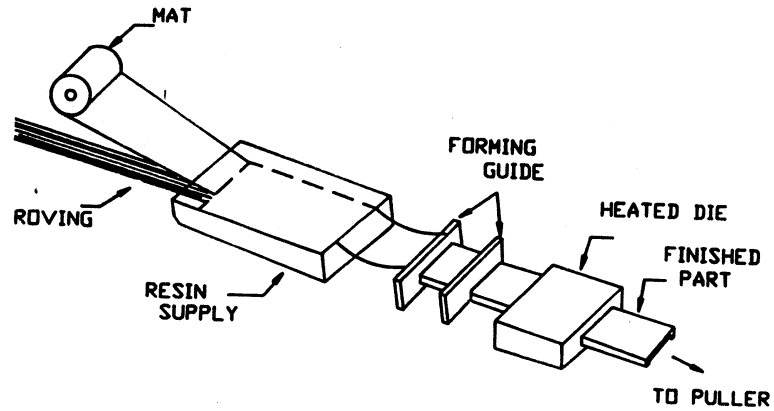

FIG. 1. Schematic of Pultrusion Process

tailored to requirements, such as corrosion resistance, and can include fire retardance and ultraviolet resistance.

Composite materials offer many advantages for the construction of public works: light weight, corrosion resistance, energy absorption, tailoring of the material to specific applications, modular construction, and ease of installation. However, the application of composite materials to infrastructures has been limited due to the lack of material properties, design methods, and allowable stresses. Some of the aspects of the design and the associated member properties have been addressed in the literature (Bank 1989). This paper addresses the ultimate load capacity of composite beams manufactured by the pultrusion process with glass fibers and polyester resins, also known as glass FRP (GFRP).

Observed Behavior

Investigation of the bending behavior of FRP beams shows that the bending stiffness is low compared to that of steel sections of the same shape. It also indicates that shear deformation effects are important. This is a consequence of the relatively low modulus of elasticity of the glass fibers (when compared to steel) and the low shear modulus of the polyester resin. Most significantly, due to the large elongation to failure allowed by both the fibers (4.0%) and the resin (4.5%), the composite material remains linearly elastic for large deflections and strains (Fu et al. 1990). This is in contrast to the cracking of concrete and plasticity of steel that occur usually with small deflections and strains.

As a consequence of the large strains to failure that can be admitted by the composite material, theoretical prediction of ultimate bending strength based on linear bending theory grossly overestimates the load-carrying capacity of the members (Barbero and Sonti 1991). However, this study shows that local buckling of the compression flange of box and I-beams occurs in the linear range of the material (top flange in Fig. 2). As a consequence of local buckling, large strains are induced during postbuckling. These large strains ultimately lead to the failure of the material (Figs. 3 and 4) and subsequent total failure of the member.

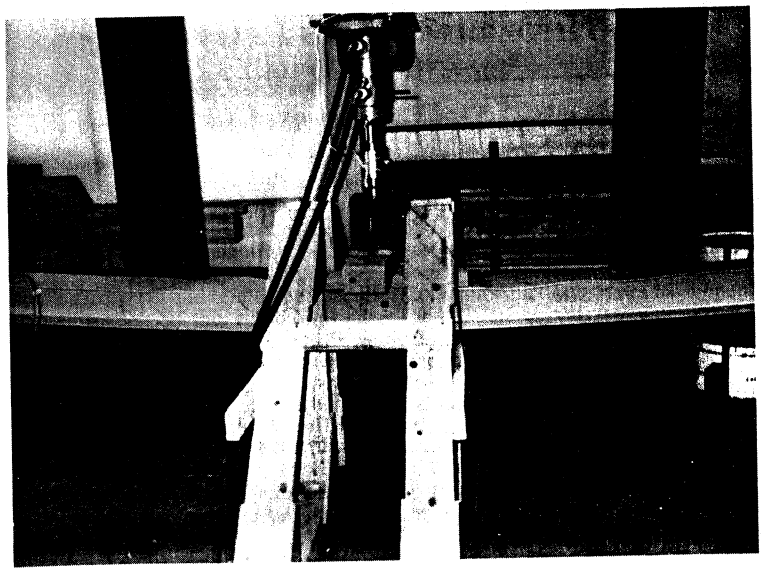

FIG. 2. Bending of FRP Beam Showing Buckled Top Flange

Experimental Results

Coupon Testing

Limited coupon testing is performed to verify the accuracy of the micromechanical models used to predict composite properties from the material properties of the constituents (fibers and resin). The samples were obtained from the flanges and webs of the beams and tested in tension (Barbero and Sonti 1991). The composite material is idealized as a laminated structure (Fig. 5); each layer approximates a portion of the cross section characterized by a particular orientation of the fibers. Even though the pultruded material is not truly laminated, it does have different fiber systems through the thickness of the flanges and webs, which justifies the laminated modeling.

Each fiber system has a particular orientation (e.g., along the axis of the beam for unidirectional roving; see Fig. 5), which influences the material properties at that particular layer, with the maximum modulus of elasticity being along the direction of the fibers. Each fiber system has also a different fiber volume fraction V_f, i.e., the percentage weight of fibers per unit weight of the composite. The fiber volume fraction also has an influence on the material properties, which can be computed using the rule of mixtures (Jones 1975) as:

$$E_1 = V_f E_f + V_m E_m \quad \ldots\ldots (1a)$$

$$E_2 = \frac{E_m E_f}{V_m E_f + V_f E_m} \quad \ldots\ldots (1b)$$

$$G_{12} = \frac{G_m G_f}{V_m G_f + V_f G_m} \quad \ldots\ldots (1c)$$

$$\nu_{12} = V_f \nu_f + V_m \nu_m \quad \ldots\ldots (1d)$$

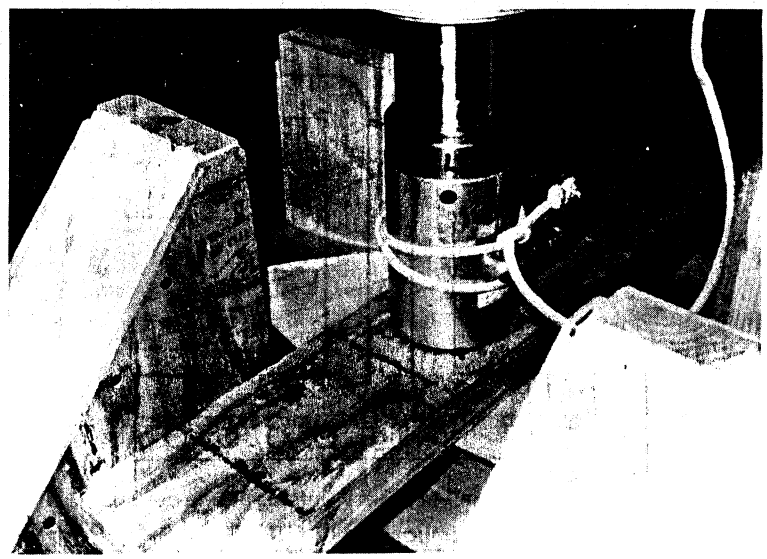

FIG. 3. First Failure of Top Flange

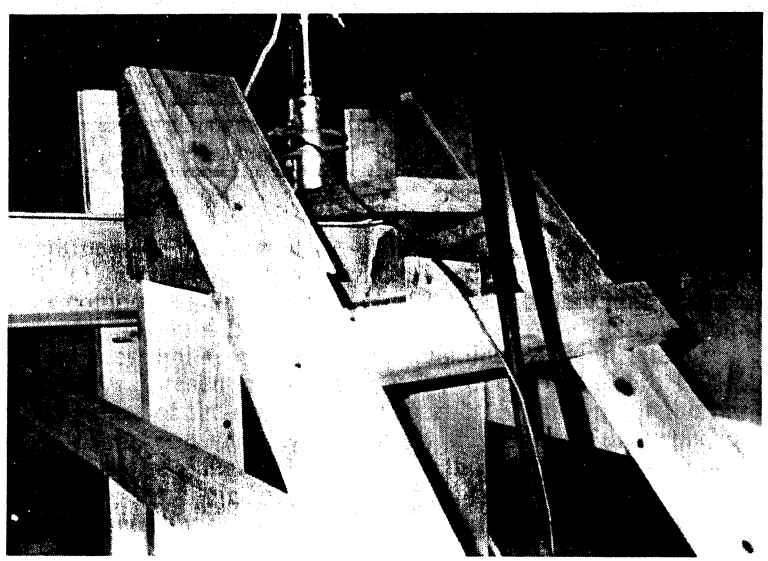

FIG. 4. Failure Propagation to Web

$$V_m = 1 - V_f \quad \ldots\ldots (1e)$$

By considering the material to be transversely isotropic on each layer (Jones 1975), only four material properties per layer are needed. E_1 and E_2 are the modulus of elasticity of the lamina along the fiber direction and transverse to it, respectively (Fig. 6). G_{12} is the in-plane shear modulus and

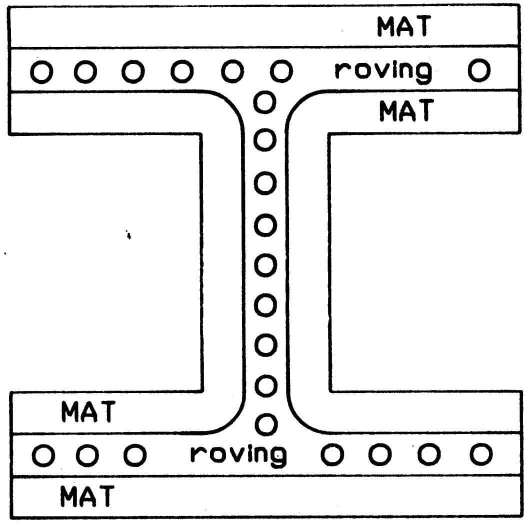

FIG. 5. Composition of FRP I-Beam

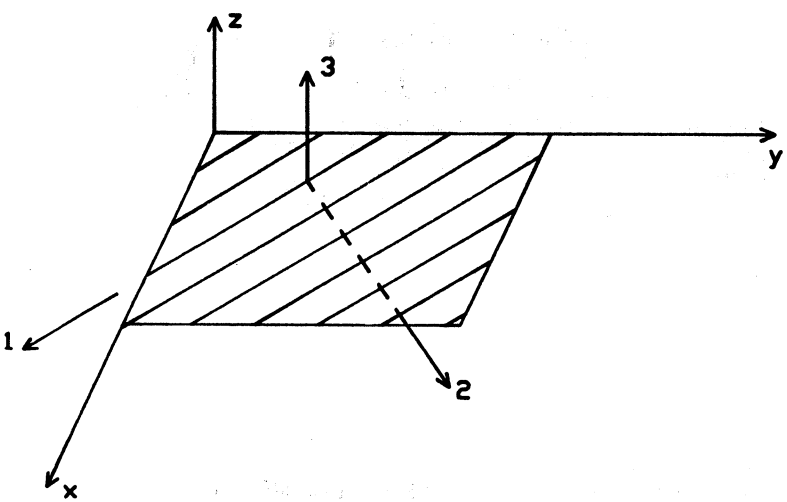

FIG. 6. Material and Structural Coordinate Systems

ν_{12} the in-plane Poisson ratio. The subscripts f and m denote fiber and matrix (resin) properties respectively.

The material properties of each layer (Fig. 5) are predicted in the material coordinate system; i.e., on a coordinate system with the one-axis oriented along the direction of the fibers, the two-axis perpendicular to the fibers, and the three-axis transverse to the thickness of the composite wall (Fig. 6). Next, the material properties for each layer are transformed to a common or global coordinate system (denoted by x,y,z in Fig. 6) with the x-axis oriented along the axis of the beam (Fig. 7). The contribution of each layer

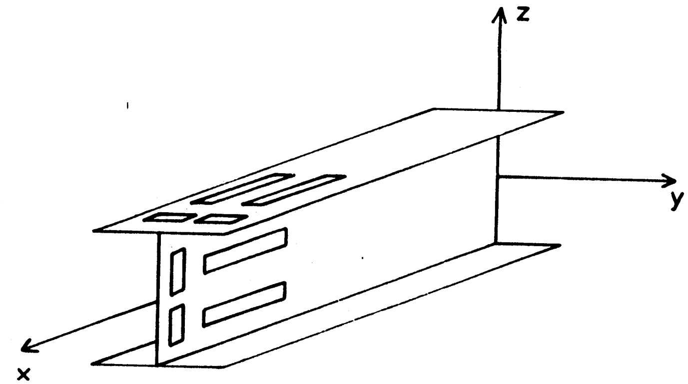

FIG. 7. Structural Coordinate System and Sample Locations

TABLE 1. Measured and Predicted Values of Equivalent Properties of Flanges of 4 × 4 box and 8 × 8 I-Beams

Case (1)	E_1[msi (GPa)] (2)	E_2[msi (GPa)] (3)	ν_{12} (4)
I-beam (measured)	2.9 (19.98)	0.85 (5.86)	0.26
I-beam (predicted)	2.74 (18.88)	0.72 (4.96)	0.27
Box beam (measured)	4.0 (27.56)	1.55 (10.68)	0.28
Box beam (predicted)	3.9 (26.87)	2.2 (15.16)	0.27

Note: These values do not necessarily represent actual properties of materials currently produced by a particular manufacturer.

to the stiffness of the composite wall are added together using classical lamination theory (Jones 1975). Finally, equivalent material properties for the entire composite wall are obtained. These equivalent material properties correspond to an equivalent homogeneous, orthotropic material that in pure tension behaves similarly to the original laminated composite.

In Table 1 we present a comparison of predicted (Barbero 1991a,b) and measured values of the equivalent properties E_1 and E_2 for the flanges of box and I-beams considered in this study. Five longitudinal specimens are cut, four from the flanges and one from the web (as shown in Fig. 7) at different positions along the length of an I-beam. They are instrumented with a 0/90 rosette for determination of E_1 and ν_{12}. Similarly, five transverse specimens are used for the determination of E_2 and ν_{12}. The following analytical relationship between these values is used to check for consistency in the experimental data:

$$\frac{E}{\nu_{12}} = \frac{E_2}{\nu_{21}} \quad \text{(2)}$$

Similarly, for the box-beam, four longitudinal and four transverse specimens cut from different locations along the axis of the beam are used to obtain the same quantities. The experimental and predicted results are summarized in Table 1. The predicted material properties of the walls of the composite

sections used in this work allows us to use analytical models developed in this work to explore alternative material configurations and to propose improvements for currently produced pultruded materials. The analytical models also allow us to get a better insight into the mechanisms of deformation and failure of pultruded composite members.

Full-Scale Testing

Three-point and four-point tests have been conducted on GFRP box and I-beams using the setup shown in Fig. 8. The specimen is supported on two concrete blocks through cylindrical rollers that simulate simply supported boundary conditions. The bending load is applied at the midspan by a remotely controlled hydraulic jack. The level of the applied load is monitored with a load cell. Dial gauges are used to measure deflections. Strain gauges are used on the top and bottom flanges as well as on the web of the beam to measure the longitudinal strains. Lateral deflections are prevented by the fixture shown in the Figs. 2, 3, 4, 8, and 10.

The test specimens are pultruded box and I-beams manufactured by Creative Pultrusions Inc., Alum Bank, Pennsylvania. They are composed of E-glass fibers and vinylester resin (*Creative Pultrusions* 1988). A total of 64 tests on I-beams and 8 tests on box beams are reported as summarized in Table 2. Typical plots of applied load versus measured deflection at the center of the beam are shown in Fig. 9 for three-point bending tests of box and I-beams of various lengths. The behavior is linear over the full range of interest. The basic structural properties that can be computed from this set of data are the equivalent bending modulus E_b and shear modulus G_b (Yu and Kincis 1985). The results are summarized in Table 3. A detailed theoretical prediction of stiffness and comparison with experimental results is presented by Barbero (1991a,b).

The equivalent moduli depend on the cross-sectional size, shape, and arrangement of the fibers. Therefore, E_b and G_b cannot be considered

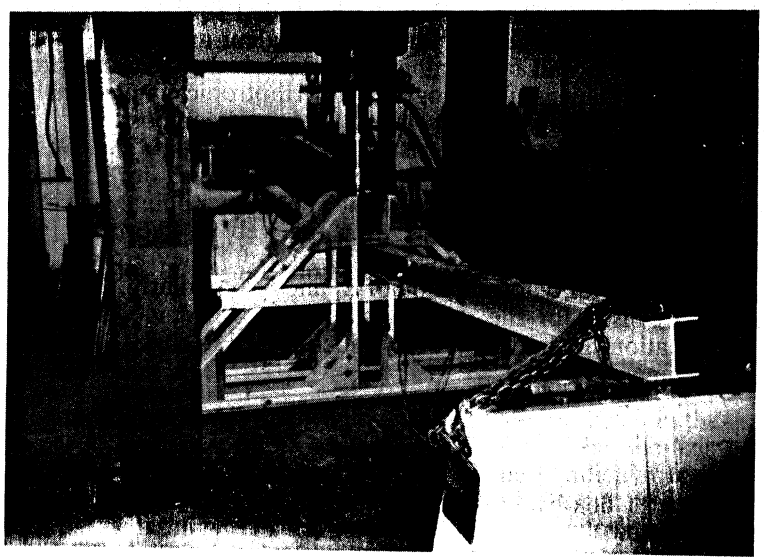

FIG. 8. Experimental Setup for Full-Scale Beam Bending

TABLE 2. Test Samples: Dimensions, Number of Tests, and Type of Tests

Cross-section dimensions (1)	Three-point test (2)	Four-point test (3)
10 × 10 × 0.43–cm box	8	—
10 × 10 × 0.64–cm WFI	10	6
15 × 15 × 0.64–cm WFI	18	6
20 × 20 × 0.95–cm WFI	10	6

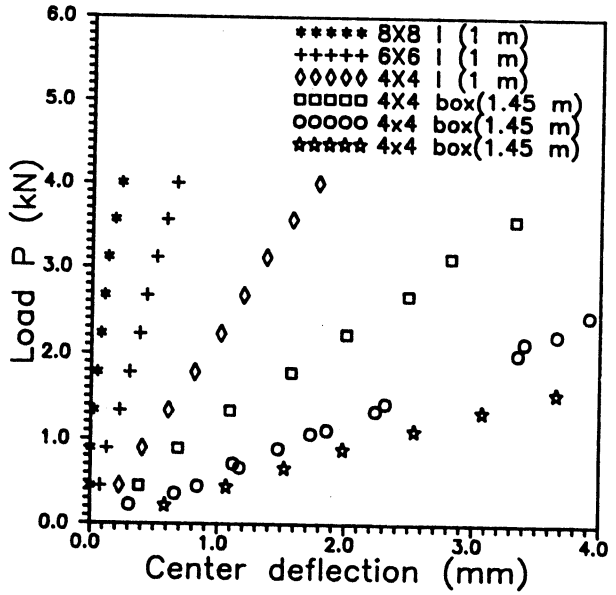

FIG. 9. Experimental Load-Deflection Data

TABLE 3. Equivalent Moduli

Cross-section dimensions (1)	E_b[msi (GPa)] (2)	G_b[msi (GPa)] (3)
10 × 10 × 0.43–cm box	2.71 (18.67)	0.0
10 × 10 × 0.64–cm WFI	2.86 (19.71)	0.16 (1.10)
15 × 15 × 0.64–cm WFI	3.06 (21.08)	0.14 (0.96)
20 × 20 × 0.95–cm WFI	2.70 (18.60)	0.17 (1.17)

Note: These values do not necessarily represent actual properties of materials currently produced by a particular manufacturer.

material properties and as a consequence, the stiffness of the member cannot be varied by simply changing the moment of inertia of the section. It is proposed in this work that the moment of inertia and the equivalent modulus be combined in a single parameter for each section. The bending stiffness

$D = E_b \cdot I$ completely characterizes the behavior of the member in bending. Similarly, to account for shear deformation, the shear stiffness $F = k \cdot G_b \cdot I$ can be used, where k is the shear correction factor.

The experimental results showed that the composite beams can experience large deformations and strains with the material remaining in the linear range. Thus, stress analysis using an appropriate failure criterion for laminated composites (Barbero and Sonti 1991) over-predicts the ultimate bending strength of the I-beams.

A 20-ft (6.1-m) I-beam shown in Fig. 8 experiences deflections beyond the capacity of the testing setup without any material degradation. However, at 1,500 lb (680 kg), the compression flange buckled in the region of maximum bending moment. The buckling wave propagates as the load increases, as shown in Fig. 2 for 2,500 lb (1,134 kg). The material remains linearly elastic up to 3,300 lb (1,496 kg) (Fig. 10), at which level the buckling wavelength of 6 in. (15 cm) is measured. With a reduced span of 11 ft (3.35 m), the postbuckling deformations become very large at 4,000 lb (1,814 kg), as shown in Fig. 3. The ultimate strain to failure of the fibers is reached at the top surface of the compression flange. Then the material fails as indicated in Fig. 3. The failure propagates for constant load to the web after a short period of time (Fig. 4).

Local Buckling Analysis

I-Beam Analysis

Bending of an I-beam produces compression on the top flange. When the critical buckling load is reached, the top flange buckles in a local mode. Each half of the flange can be modeled as a plate elastically supported by the web and free at the edge. Due to the periodic form of the buckling wave along the length of the beam, the flange can be assumed to be simply supported at any of the inflection points of the buckling wave. Three cases

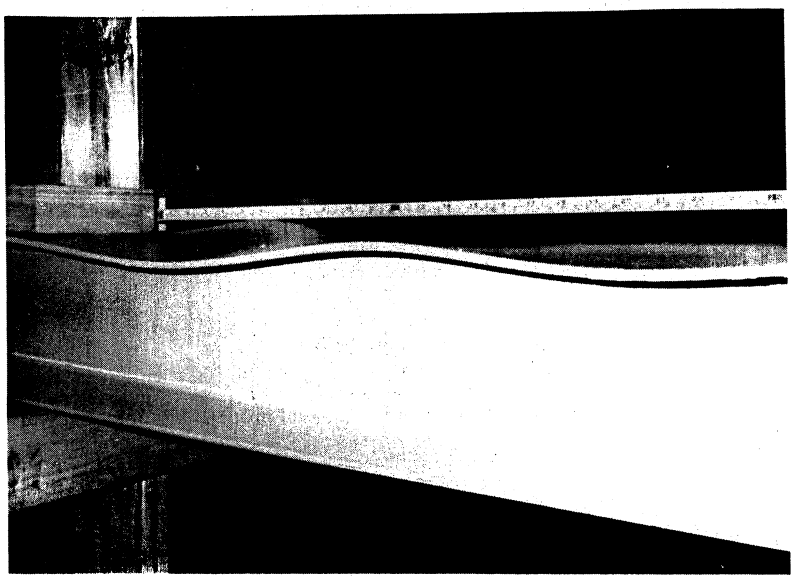

FIG. 10. Postbuckling Shape of Top Flange

of the elastically clamped edge are examined here: flexible flange-web connection, rigid flange-web connection, and hinged flange-web connection.

For a laminated composite plate without bending-extension or bending-twisting coupling, the governing equation (Jones 1975) is

$$D_{11}\frac{\partial^4 w}{\partial x^4} + 2(D_{12} + 2D_{66})\frac{\partial^4 w}{\partial x^2 \partial y^2} + D_{22}\frac{\partial^4 w}{\partial y^4} + N_x\frac{\partial^2 w}{\partial x^2} = 0 \quad \ldots\ldots (3)$$

where $w(x,y)$ = the deformed shape of the plate of length a, when buckling occurs, and can be represented by the function

$$w(x,y) = \sum_{m-1}^{\infty} f_m(y) \sin\frac{m\pi x}{a} \quad \ldots\ldots (4)$$

which, when substituted into (3) for a specific mode number m, gives

$$D_{22}\frac{\partial^4 f_m}{\partial y^4} - 2(D_{12} + 2D_{66})\left(\frac{m\pi}{a}\right)^2\frac{\partial^2 f_m}{\partial y^2} + \left[\left(\frac{m\pi}{a}\right)^4 D_{11} - N_x\left(\frac{m\pi}{a}\right)^2\right] f_m = 0 \quad \ldots\ldots (5)$$

The characteristic equation of (5) is

$$f^4 - 2D_2\left(\frac{m\pi}{a}\right)^2 f^2 + \left[D_3\left(\frac{m\pi}{a}\right)^4 - k\left(\frac{m\pi}{a}\right)^2\right] = 0 \quad \ldots\ldots (6)$$

where

$$D_2 = \frac{(D_{12} + 2D_{66})}{D_{22}}; \qquad D_3 = \frac{D_{11}}{D_{22}}; \qquad k = \frac{N_x}{D_{22}} \quad \ldots\ldots (7)$$

Since the critical load for a plate supported on one side is always larger than the critical load for a wide column (Brush and Almroth 1975), we can take

$$k > D_3\left(\frac{m\pi}{a}\right)^2 \quad \ldots\ldots (8)$$

Therefore, (6) has two real and two imaginary roots:

$$f = \pm\alpha, \pm\beta \quad \ldots\ldots (9a)$$

$$\alpha = \left\{D_2\left(\frac{m\pi}{a}\right)^2 + \left(\frac{m\pi}{a}\right)\left[(D_2^2 - D_3)\left(\frac{m\pi}{a}\right)^2 + k\right]^{1/2}\right\}^{1/2} \quad \ldots\ldots (9b)$$

$$\beta = \left\{-D_2\left(\frac{m\pi}{a}\right)^2 + \left(\frac{m\pi}{a}\right)\left[(D_2^2 - D_3)\left(\frac{m\pi}{a}\right)^2 + k\right]^{1/2}\right\}^{1/2} \quad \ldots\ldots (9c)$$

Therefore, $f_m(y)$ in (4) becomes

$$f_m(y) = A \sinh \alpha y + B \cosh \alpha y + E \sin \beta y + F \cos \beta y \quad \ldots\ldots (10)$$

Plate Elastically Supported at $y = 0$

The boundary conditions for the flange, elastically supported at the web are

$$w(0,y) = 0; \quad w(a,y) = 0; \quad M_x(0,y) = 0; \quad M_x(a,y) = 0 \quad \ldots (11a)$$

$$w(x,0) = 0; \quad M_y(x,0) = -d\frac{\partial w}{\partial y}; \quad M_y(x,b) = 0;$$

$$Q_y(x,b) = 0 \quad \ldots (11b)$$

where d = the elastic constant of the support; M_x and M_y = the bending moments; and Q_y = the shear force at the support. The first boundary condition yields $B + F = 0$, which, when substituted in the second boundary condition, yields

$$d\alpha A - D_{22}^2(\alpha^2 + \beta^2)B + d\beta E = 0 \quad \ldots (12)$$

The third boundary condition yields

$$A\left[D_{22}\alpha^2 - \left(\frac{m\pi}{a}\right)^2 D_{12}\right] \sinh \alpha b + B\left[D_{22}(\alpha^2 \cosh \alpha b + \beta^2 \cos \beta b) - D_{12}\left(\frac{m\pi}{a}\right)^2 (\cosh \alpha b - \cos \beta b)\right] - E\left[D_{12}\left(\frac{m\pi}{a}\right)^2 + D_{22}\beta^2\right] \sin \beta b = 0 \quad \ldots (13)$$

The fourth boundary condition yields

$$A\left[\alpha^3 D_{22} - (D_{12} + 4D_{66})\left(\frac{m\pi}{a}\right)^2 \alpha\right] \cosh \alpha b + B\left[D_{22}(\alpha^3 \sinh \alpha y - \beta^3 \sin \beta y) - (D_{12} + 4D_{66})\left(\frac{m\pi}{a}\right)^2 (\alpha \sinh \alpha b + \beta \sin \beta b)\right] - E\left[D_{22}\beta^3 \cos \beta b + \beta(D_{12} + 4D_{66})\left(\frac{m\pi}{a}\right)^2 \cos \beta b\right] = 0 \quad \ldots (14)$$

Eqs. (12), (13), and (14) form a linear homogeneous system of three equations. For a nontrivial solution we set the determinant to zero, which gives an eigenvalue problem from which we can obtain the buckling load and buckling shape.

Plate Clamped at $y = 0$

In this case the elastic constant d approches infinity. Therefore, we divide all the terms of (12) by d, which leads to

$$\alpha A + \beta E = 0 \quad \ldots (15)$$

Plate Simply Supported at $y = 0$

In this case, the elastic constant of the support is $d = 0$, which simplifies even further the system of (12), (13), and (14).

Box-Beam Analysis

Due to the symmetric construction of a box beam, any side can be subjected to compression during bending. The flange can be modeled as a plate

elastically supported by two webs. Due to the periodic form of the buckling wave along the length of the beam, the flange can be assumed to be simply supported at any of the inflection points of the buckling wave. Three cases of the elastically clamped edge are examined here: flexible flange-web connection, rigid flange-web connection, and hinged flange-web connection. The boundary conditions are

$$w(x,0) = 0 \quad \ldots (16a)$$

$$w(x,b) = 0 \quad \ldots (16b)$$

$$M_y(x,0) = -d_1\frac{\partial w}{\partial y} \quad \ldots (16c)$$

$$M_y = d_2\frac{\partial w}{\partial y} \quad \ldots (16d)$$

where d_1 and d_2 = the stiffness of the webs. The solution is taken in the form of (4) and (10). The first boundary condition gives $B + F = 0$. The second boundary condition gives:

$$A \sinh \alpha b + B(\cosh \alpha b - \cos \beta b) + E \sin \beta b = 0 \quad \ldots (17)$$

The third boundary condition gives

$$d_1\alpha A - D_{22}(\alpha^2 + \beta^2)B + d_1\beta E = 0 \quad \ldots (18)$$

and the fourth boundary condition gives

$$A[D_{22}\alpha^2 \sinh \alpha b + d_2\alpha \cosh \alpha b] + B[D_{22}(\alpha^2 \cosh \alpha b + \beta^2 \cos \beta b) + d_2(\alpha \sinh \alpha b + \beta \sin \beta b)] - E[D_{22}\beta^2 \sin \beta b - d_2\beta \cos \beta b] = 0 \quad \ldots (19)$$

Eqs. (17), (18), and (19) form a linear homogeneous system of three equations. For a nontrivial solution, we set the determinant to zero, which gives an eigenvalue problem from which we can obtain the buckling load and buckling shape.

Correlation with Observed Behavior

The analytical solutions so far developed are used to model the members for which full-scale testing in bending is reported. We used predicted equivalent properties for the material of the flanges and webs of the members. However, we could as well have used the measured properties obtained by coupon testing, because the predicted and measured values correlate very well (Table 1). It is significant that by using predicted properties, we can use the analytical model to predict the behavior of all currently produced sections (in excess of 250 for one manufacturer alone) without extensive coupon testing. We can also predict the behavior of suggested material combinations not being produced yet, to evaluate the merits of different options (Barbero and Raftoyiannis 1990; Fu et al. 1990).

In Fig. 11 we show the critical buckling load of the compression flange of a 6 × 6 I-beam as a function of the wavelength. For a short wavelength, the flange buckles in mode one ($m = 1$), i.e., in the shape of sin ($m\pi/a$). The critical load reaches a minimum for a wave length of 6 in. (15 cm)

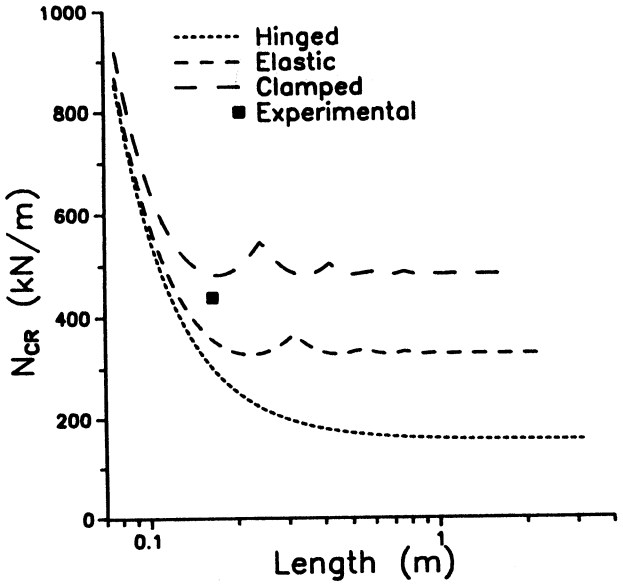

FIG. 11. Local Buckling Load of Top Flange of I-Beam

(dashed line in Fig. 11). For a longer wavelength, the mode number increases but the minimum critical load is constant. This implies that the wavelength is irrelevant, which supports our assumption of a simply supported boundary at the inflection points along the length of the beam. It also implies that the local buckling of the compression flange is independent of the length of the beam and only dependent on the maximum bending moment applied. All these observations agree with the observed behavior in the full-scale experimental program. The predicted wavelength of 6 in. (15 cm) agrees with the measured wavelength of 6 in. (15 cm) in Fig. 10.

Three different boundary conditions were used to simulate the support provided to the flange by the web. The clamped boundary condition seems to model the observed behavior more accurately than a hinged or elastically supported flange. This is because the web thickens near the intersection with the flange. For the elastic support we use the bending stiffness D_{22} of the web.

The critical load reported in Fig. 11 is the stress resultant value acting on the flange. This value translated to actual bending moment on the beam overpredicts by 15% (for clamped flange), the value for which buckling initiation was observed (Fig. 11). The elastically supported boundary prediction correlates better. However, the influence of initial imperfections are certainly the cause for this minor discrepancy.

In Fig. 12 we show the critical buckling load of the compression flange of a 4 × 4 box beam as a function of the wavelength. Three different boundary conditions were used to simulate the support provided to the flange by the webs. For the elastic support we use the bending stiffness D_{22} of the webs.

Even though the model used for the box and I-beam are entirely different, both predict the same type of results; namely, that the local buckling load is independent of the wavelength. As the experiments demonstrate, local

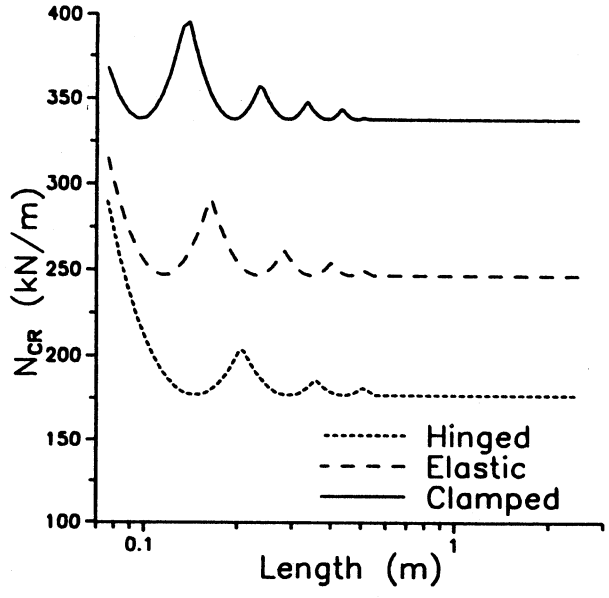

FIG. 12. Local Buckling Load of Top Flange of Box Beam

buckling of the compression flanges initiates a process that leads to the collapse of the member. Prediction of local buckling is therefore crucial for the prediction of ultimate bending strength of the pultruded beams in bending.

Conclusions

Excellent correlation between analytical and experimental results are obtained. It is demonstrated that the ultimate bending strength of GFRP beams is reached as a consequence of local buckling of the compression flange. The buckling load can be accurately estimated by the analytical models developed here. The usefulness of micromechanical analyses is demonstrated. Application of the analytical model to optimization of the material will be presented in a related paper.

Acknowledgment

The writers wish to thank Hota GangaRao, director of the Constructed Facilities Center at West Virginia University, Morgantown, West Virginia, for providing valuable suggestions to this work. The contribution of Costantine Spyrakos and Jacky Prucz are also acknowledged. This research was performed under National Science Foundation grant 8802265 and West Virginia Department of Highways RPT699. The financial support and comments of the monitor J. B. Scalzi are also gratefully acknowledged. Special recognition is given to Creative Pultrusions, Inc., Alum Bank, Pennsylvania, for providing the materials used in the experimental program.

Appendix I. Refferences

Bank, L. C. (1989). "Properties of pultruded fiber reinforced plastic structural members." *68th Annual Meeting*, Transportation Research Board, 1–15.

Barbero, E. J. (1991a). "Pultruded structural shapes—from the constituents to the structural behavior." *Soc. for the Advancement of Mater. and Process Engrg.*, 27(1), 25–30.
Barbero, E. J., and Raftoyiannis, I. (1990). "Buckling analysis of pultruded composite columns," ASME Winter Annual Meeting, American Society of Mechanical Engineers, 47–52.
Barbero, E. J. (1991b). "Pultruded structural shapes: Stress analysis and failure prediction." *Advanced composite materials in civil engineering structures*, S. L. Iyer, ed., ASCE, New York, N.Y., 194–204.
Barbero, E. J., and Sonti S. (1991). "Micro-mechanical modeling for pultruded composite beams," presented at the 32nd Structural Dynamics Conference, American Institute of Aeronautics and Astronautics, Baltimore, Md.
Brush, D. O., and Almroth, B. O. (1975). *Buckling of bars, plates, and shells*. McGraw Hill, New York, N.Y.
Creative pultrusions design manual. (1988). Creative Pultrusions Inc., Alum Bank, Pa.
Fu, S. H., Spyrakos, C., Prucz, J., and Barbero, E. J. (1990). "Structural performance of plastic I-beams." *Eighth Annual Structures Congress*, ASCE, 507–508.
Jones, R. M. (1975). *Mechanics of composite materials*. Hemisphere Publishing Corp., New York, N.Y.
Yu, M. T., and Kincis, T. (1985). *Static test methods for composites*. 3rd Ed., George Lubin, ed., Van Nostrand Reinhold Co., New York, N.Y.

New Method for Measuring Pore Size Distributions in Concrete

By Brett W. Gunnink,[1] Associate Member, ASCE

Abstract: A new method for measuring the pore size distributions (PSDs) of saturated porous materials has been developed. With this new methodology, referred to as conductometric phase transition porosimetry (CPTP), the changes in electrical conductance and temperature of saturated porous materials that have been subjected to a cycle of capillary freezing and melting are measured and used to calculate PSD. Based on this methodology, a porosimeter was constructed. Methods and procedures for determining the PSD of 4-in. (10.6-cm) diameter by 4-in. (10.6-cm) high portland cement mortar and concrete cylinders are introduced. The CPTP method has been found to be free of the problems of entrapment of mercury inherent to mercury porosimetry. Also, the pressures a sample is subjected to during testing are much less than those necessary with mercury porosimetry. Therefore, deformation or destruction of pores is less. It is well known that for many geomaterials, pore structure is dependent on moisture content. With CPTP, samples do not have to be dried prior to testing as with other techniques.

Introduction

A new method for measuring pore volume–pore size relationships (pore size distributions) of porous materials has been developed. This new methodology has been referred to as conductometric phase transition porosimetry (CPTP). The inventors of this new methodology have previously identified (Gunnink et al. 1988) two significant advantages that CPTP has over other available porosimetry methods. These include the minimal sample preparation necessary with CPTP, which results in less disturbance of the sample's pore structure during testing, and the ability to determine pore size distributions of large samples, much larger than those other porosimeters can test, which minimizes sampling errors. Because of these advantages, CPTP is especially well suited for the analysis of heterogeneous water-sensitive materials including soils, aggregates, and concretes. The purpose of this paper is to introduce an experimental method that has been developed for the determination of the pore size distribution (PSD) of portland cement concrete cylinders.

The determination of PSD is important in the characterization of a wide variety of materials. Two independent methods have found large-scale application for PSD analysis. The first is mercury porosimetry. Two problems associated with this method have not been solved satisfactorily: (1) The mercury/matrix contact angle; and (2) the entrapment of mercury during extrusion. The second method, the capillary condensation method, makes use of the well-known Kelvin equation. It is an elaborate and time-consuming method, and results vary with the adsorbate used. With each method, it is necessary to dry samples as part of the test. Also, each is capable of testing small-size samples only (1 or 2 g).

Recently, several methods have been introduced that allow the testing of

[1]Asst. Prof., Dept. of Civ. Engrg., Univ. of Missouri–Columbia, Columbia, MO 65211.

Note. Discussion open until April 1, 1992. To extend the closing date one month, a written request must be filed with the ASCE Manager of Journals. The manuscript for this paper was submitted for review and possible publication on June 1, 1989. This paper is part of the ***Journal of Materials in Civil Engineering***, Vol. 3, No. 4, November, 1991. ©ASCE, ISSN 0899-1561/91/0004-0307/$1.00 + $.15 per page. Paper No. 26383.